Check for updates

ADVANCED ELECTRONIC MATERIALS
www.advelectronicmat.de

Beyond the 2D Field-Effect Charge Transport Paradigm in Molecular Thin-Film Transistors

Emilia Benvenuti, Giuseppe Portale, Marco Brucale, Santiago D. Quiroga, Matteo Baldoni, Roderick C. I. MacKenzie, Francesco Mercuri, Sofia Canola, Fabrizia Negri, Nicolò Lago, Marco Buonomo, Andrea Pollesel, Andrea Cester, Massimo Zambianchi, Manuela Melucci, Michele Muccini, and Stefano Toffanin**

Organic field-effect transistors (OFETs) are considered almost purely interfacial devices with charge current mainly confined in the first two semiconducting layers in contact with the dielectric with no active role of the film thickness exceeding six to eight monolayers (MLs). By a combined electronic, morphological, structural, and theoretical investigation, it is demonstrated that the charge mobility and source–drain current in 2,20-(2,20-bithiophene-5,50-diyl)bis(5-butyl-5*H*-thieno[2,3-*c*]pyrrole-4,6)-dione (NT4N) organic transistors directly correlate with the out-of-plane domain size and crystallite orientation in the vertical direction, well beyond the dielectric interfacial layers. Polycrystalline films with thickness as high as 75 nm (≈30 MLs) and 3D molecular architecture provide the best electrical and optoelectronic OFET characteristics, highlighting that the molecular orientational order in the bulk of the film is the key-enabling factor for optimum device performance. X-ray scattering analysis and multiscale simulations reveal the functional correlation between the thickness-dependent molecular packing, electron mobility, and vertical charge distribution. These results call for a broader view of the fundamental mechanisms that govern field-effect charge transport in OFETs beyond the interfacial 2D paradigm and demonstrate the unexpected role of the out-of-plane domain size and crystallite orientation in polycrystalline films to achieve optimum electronic and optoelectronic properties in organic transistors.

1. Introduction

Field-effect transistors became ubiquitous in practically all technologies impacting our lives, such as health diagnostics and therapeutics, production, earth and environment monitoring, space, transportation, energy, digital technologies, etc.[1–4]

Organic field-effect transistors (OFETs) provide a platform that breaks through the limits of FET technology by enabling lightweight, flexible, and transparent devices integrated in practically any substrate and system.[5] The heart of the OFET is the thin film of organic material that acts as the semiconductor layer in contact with the dielectric and charge injecting contacts. OFETs are considered almost purely interface devices, i.e., the few molecular layers at the organic/dielectric interface are considered to determine the nature and efficacy of charge transport in the transistor channel along a direction parallel to the substrate. Indeed, charge current has been reported to be mainly confined in the first

E. Benvenuti, M. Brucale, S. D. Quiroga, M. Baldoni, F. Mercuri, M. Muccini, S. Toffanin
Istituto per lo Studio dei Materiali Nanostrutturati
Consiglio Nazionale delle Ricerche (CNR-ISMN)
Via Gobetti 101, Bologna 40129, Italy
E-mail: michele.muccini@cnr.it; stefano.toffanin@cnr.it

G. Portale
Zernike Institute for Advanced Materials Micromechanics
University of Groningen
Nijenborgh 4, Groningen 9747AG, The Netherlands

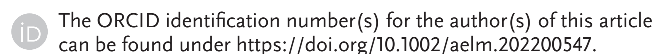
The ORCID identification number(s) for the author(s) of this article can be found under https://doi.org/10.1002/aelm.202200547.

© 2022 The Authors. Advanced Electronic Materials published by Wiley-VCH GmbH. This is an open access article under the terms of the Creative Commons Attribution License, which permits use, distribution and reproduction in any medium, provided the original work is properly cited.

[+]Present address: Institute of Physics of the Czech Academy of Sciences, Cukrovarnická 10/112, CZ16200, Praha 6, Czech Republic.

DOI: 10.1002/aelm.202200547

R. C. I. MacKenzie
Department of Engineering
Durham University
Lower Mount Joy
South Road, Durham DH1 3LE, UK

S. Canola,[+] F. Negri
Dipartimento di Chimica "Giacomo Ciamician,"
Università di Bologna
Italy and INSTM
UdR Bologna
Via F. Selmi 2, Bologna 40126, Italy

N. Lago, M. Buonomo, A. Pollesel, A. Cester
Dipartimento di Ingegneria dell'Informazione
Università di Padova
Via Gradenigo 6B, Padova 35131, Italy

M. Zambianchi, M. Melucci
Istituto per la Sintesi Organica e la Fotoreattività
Consiglio Nazionale delle Ricerche (CNR-ISOF)
Via Gobetti 101, Bologna 40129, Italy

2199160x, 2023, 1, Downloaded from https://onlinelibrary.wiley.com/doi/10.1002/aelm.202200547 by Test, Wiley Online Library on [15/03/2023]. See the Terms and Conditions (https://onlinelibrary.wiley.com/terms-and-conditions) on Wiley Online Library for rules of use; OA articles are governed by the applicable Creative Commons License

ADVANCED ELECTRONIC MATERIALS
www.advelectronicmat.de

two semiconducting layers in contact with the dielectric[6–8] and to saturate at a thickness of about six monolayers (MLs).[9–12] It is generally assumed that laterally extended layered film structures, instead of 3D island-like granular structures, provide the ideal configuration to achieve high charge carrier mobility and current intensity.[13,14] For this reason, great effort has been spent in searching ways to fabricate high-quality layered thin films (or even ML molecular crystals[15–18]) and in correlating the morphology and structure of organic films to the carrier mobility. However, film texture, grain size, grain connectivity, and molecular packing are highly complex features and strictly dependent on intermolecular interactions, deposition methodologies, and conditions,[19] which typically prevent the disclosure of the intrinsic properties of the used organic semiconductors and the straightforward correlation between solid-state structure and functional properties in thin films. In this perspective, the ultimate reference model for organic semiconductor systems to be used as active layer in OFET is the single crystal. Indeed, the absence of grain boundaries and defects, and the long-range periodic order reveal the intrinsic charge transport properties of organic semiconductors.[20] Within the purely interfacial view, the electron traps present at the semiconductor–dielectric interface play a crucial role to decrease charge mobility and to hinder the intrinsic charge transport capabilities of the semiconductors. A breakthrough occurred when it was demonstrated that in OFETs trapping of electrons at the semiconductor–dielectric interface mainly occurs by hydroxyl groups, present in the form of silanols in the case of the commonly used SiO_2 dielectric, and that hydroxyl-free gate dielectrics can yield n-channel FET conduction in most conjugated polymers.[21]

Building on the assumption that OFETs are purely interfacial devices, recent trends aim at shrinking the active layer thickness to few molecular layers, or even MLs, to achieve better charge transport properties. However, inferior mobilities are obtained for ML or ultrathin (a few layer in thickness) devices while comparable performance to bulk-film devices could be obtained when the film thickness reached a critical value.[15] Thus, many open questions remain to understand the detailed mechanisms of charge transport and the factors that determine the electrical properties of OFETs. For example, it has not yet been clearly demonstrated that a transition from 2D to 3D growth modes in organic molecular systems, which is typically correlated with the increase of the thickness of the device active layer, is the origin of the limitation in charge carrier mobility, once all other factors, like charge injection contacts[22] and chemical traps[23] and impurities,[24] are put under control. There is therefore the need to address the topic of charge transport in molecular thin-film transistors by widening the investigations to other possible key-enabling factors (such as out-of-plane domain size and crystallite orientation) determining charge transport and the other optoelectronic properties of OFETs. Indeed, one of the attractive features of the OFET platform is the possibility to integrate in a single device both the switching and amplification properties and the light emission capability to generate light-emitting field-effect transistors (OLETs).[25] Ambipolar OLETs are truly multifunctional devices, whose characteristics strictly depend on the properties of the semiconducting thin film used as active layer of the transistor.[26] The field-effect charge transport and the emissive radiative processes might be considered as cross-correlate (or even self-excluding) functional properties in polycrystalline films comprised by organic semiconductors, which eventually must be optimized within the same device region in OLET channels.[27–29] Therefore, a deep insight into the rules governing the relationship between structural and morphological semiconducting film properties and field-effect charge transport as the thin-film thickness is increased, is essential also to identify the molecular systems that are best suitable for OLETs.

Recently, the small-molecule 2,20-(2,20-bithiophene-5,50-diyl)bis(5-butyl-5*H*-thieno[2,3-*c*]pyrrole-4,6)-dione, namely NT4N (**Figure 1**a), has been synthetized and processed in thin film.[30] This material shows ambipolar charge transport and electroluminescence properties when used in OLET device structures,[31] close crystal packing, and function-specific polymorphism properties.[32] Such unique features can be likely ascribed to the thienoimide end-groups that impart to NT4N a structural rigidity and typical packing motif of acenes (favorable to charge transport), but also allow thienyls interring rotation as in α–α linked oligothiophenes.[33] NT4N single crystal shows

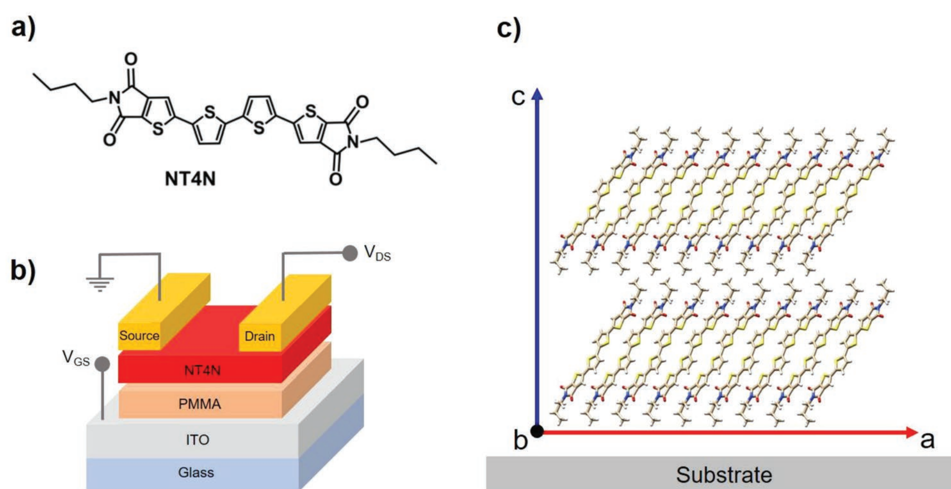

Figure 1. a) Chemical structure of NT4N organic semiconductor, b) schematic representation of the BG/TC OLET architecture and c) molecular packing of NT4N in the crystalline β phase expected in polycrystalline thin films.

© 2022 The Authors. Advanced Electronic Materials published by Wiley-VCH GmbH

2199160x, 2023, 1, Downloaded from https://onlinelibrary.wiley.com/doi/10.1002/aelm.202200547 by Test, Wiley Online Library on [15/03/2023]. See the Terms and Conditions (https://onlinelibrary.wiley.com/terms-and-conditions) on Wiley Online Library for rules of use; OA articles are governed by the applicable Creative Commons License

ADVANCED ELECTRONIC MATERIALS
www.advelectronicmat.de

π–π stacking packing mode—instead of the herringbone motif typical of oligothiophenes—with the molecules of adjacent π–π stacks engaged in supramolecular 1D network based on the intermolecular C—H···O—H interaction.[34]

Interestingly, vacuum-sublimed films show the same crystalline packing modality observed in single crystal[30] together with ambipolar charge transport, high electron mobility, and electroluminescence in OLETs. The concomitant occurrence of standard layer-by-layer growth at low film-thickness and the 3D growth modality with preserved crystalline structure in films of increasing thickness, makes this molecule an excellent model for addressing the question of whether the molecular field-effect transistors are intrinsically purely interfacial devices, or a more complex view beyond 2D must be considered to thoroughly rationalize charge transport and light emission in OFETs.

Here, we report on the functional correlation between the field-effect charge transport and the out-of-plane domain size and crystallite orientational order and vertical charge-carrier distribution in OFETs based on NT4N thin films with thickness varying from 1 to 100 nm. By combining nanoscale optical and surface-sensitive scattering probes such as grazing incidence small- and wide-angle X-ray scattering (GISAXS and GIWAXS) and atomic force microscopy (AFM), we identify the unexpected correlation between the device figures of merit (i.e., charge carrier mobility and source–drain current) and the conservation of a high degree of molecular alignment along the direction normal to the substrate. We discover that the major driving force in maximizing field-effect charge transport in organic multifunctional transistors is the molecular alignment and crystalline order across the film thickness. The cross-correlation of extensive structural analysis by means of X-ray scattering and two-step multiscale simulations provides a deep insight into the thickness-dependent molecular packing and vertical charge distribution that enables electron mobility of the order of 1 $cm^2 V^{-1} s^{-1}$.

2. Results and Discussion

We collected the optoelectronic response of ambipolar NT4N-based OLETs in bottom-gate/top-contact (BG/TC) configuration by systematically varying the nominal thickness (Θ) of the organic active layer in the range 1–100 nm. Figure 1 shows a scheme of the device architecture used in this work, the NT4N molecular structure, and the crystal packing motif expected in vacuum-sublimed thin films.[32]

A summary of the major optoelectronic parameters of devices with varying thickness of the active layer is reported in **Table 1**. All reported values are averaged on a large number of devices (>100 OLETs) to improve the statistics and the reliability of the analysis.

The mobility (μ) and threshold voltage (V_{th}) for both electrons and holes were extracted for all the devices at varying active-layer thickness by using the locus-characteristics in order to separate unambiguously the ambipolar and saturation-unipolar regimes.

By comparing all the values extracted from the optoelectronic characteristics, it is evident that the electron mobility (μ_e) is at least two-order-of-magnitude higher than the hole mobility (μ_h) regardless of the film thickness, as previously reported.[31] We observe that both electron and hole mobility values increase as the thickness of the transistor active layer increases reaching maximum values at a thickness higher than 50 nm. Indeed, the ratio between the n-type and p-type mobility is almost invariant with the layer thickness (see column μ_e/μ_h in Table 1). Interestingly, both electron and hole mobilities increase of more than one order of magnitude passing from $\Theta = 15$ nm to $\Theta = 50$ nm. Noteworthy, with increasing the NT4N thickness V_{th} decreases in the case of electron conduction, while this variation is negligible for hole conduction.

In order to shed light on the mechanisms that promote the improvement of the device optoelectronic performance by increasing the active layer thicknesses, we first quantify the contact resistance (R_C) at the Au electrodes/NT4N interface, and consequently the OLET channel resistance (R_{Ch}), as the NT4N layer thickness is increased (see Figure S2 in the Supporting Information).[35] R_{Ch} values are hundred times higher than the corresponding R_C values, regardless of the specific layer thickness, moreover, R_C decreases with the increase of Θ. This unexpected behavior is consistent with other findings showing the inverse proportionality between mobility and contact resistance,[36,37] thus reflecting the improvement of the

Table 1. Optoelectronic properties of NT4N-based BG/TC OLETs with different active layer thickness. In order to improve measurement's reliability, all parameters were averaged on a statistically significant number of devices. Charge carrier mobility and threshold voltage are indicated as μ_e, V_{th}^n, and μ_h, V_{th}^p in case of n-type polarization and of p-type polarization, respectively. The ratio between electron and hole mobility is also reported. Both μ and V_{th} were evaluated in the saturation regime by collecting the locus characteristics (i.e., V_{GS} and V_{DS} simultaneously varying with $V_{GS} = V_{DS}$, where V_{GS} is the gate–source voltage and V_{DS} is the drain–source voltage). All the values for maximum drain–source current (I_{DS}^{max}) and for emitted optical power (EL) were collected on OLETs applying $V_{GS} = 100$ V and $V_{DS} = 100$ V.

Thickness Θ [nm]	Charge mobility			Threshold voltage		I_{DS}^{max} [mA]	EL@100V [nW]
	μ_e [$cm^2 V^{-1} s^{-1}$]	μ_p [$cm^2 V^{-1} s^{-1}$]	μ_e/μ_p	V_{th}^n [V]	V_{th}^p [V]		
10	8.6×10^{-3}	–	–	64.2	–	1.0×10^{-2}	–
15	3.1×10^{-2}	8.3×10^{-5}	3.7×10^{2}	51.9	–68.6	7.0×10^{-2}	–
30	8.4×10^{-2}	2.5×10^{-4}	3.4×10^{2}	49.1	–68.8	1.2×10^{-1}	–
50	5.1×10^{-1}	1.7×10^{-3}	3×10^{2}	49.8	–67.4	9.7×10^{-1}	1.7
62	7.4×10^{-1}	1.4×10^{-3}	5.3×10^{2}	44.0	–66.5	1.3	4.1
75	7.5×10^{-1}	1.2×10^{-3}	6.3×10^{2}	41.0	–67.6	1.4	5.2
100	5.3×10^{-1}	1.0×10^{-3}	5.3×10^{2}	29.7	–65.6	1.4	6.2

© 2022 The Authors. Advanced Electronic Materials published by Wiley-VCH GmbH
2199160x, 2023, 1, Downloaded from https://onlinelibrary.wiley.com/doi/10.1002/aelm.202200547 by Test, Wiley Online Library on [15/03/2023]. See the Terms and Conditions (https://onlinelibrary.wiley.com/terms-and-conditions) on Wiley Online Library for rules of use; OA articles are governed by the applicable Creative Commons License

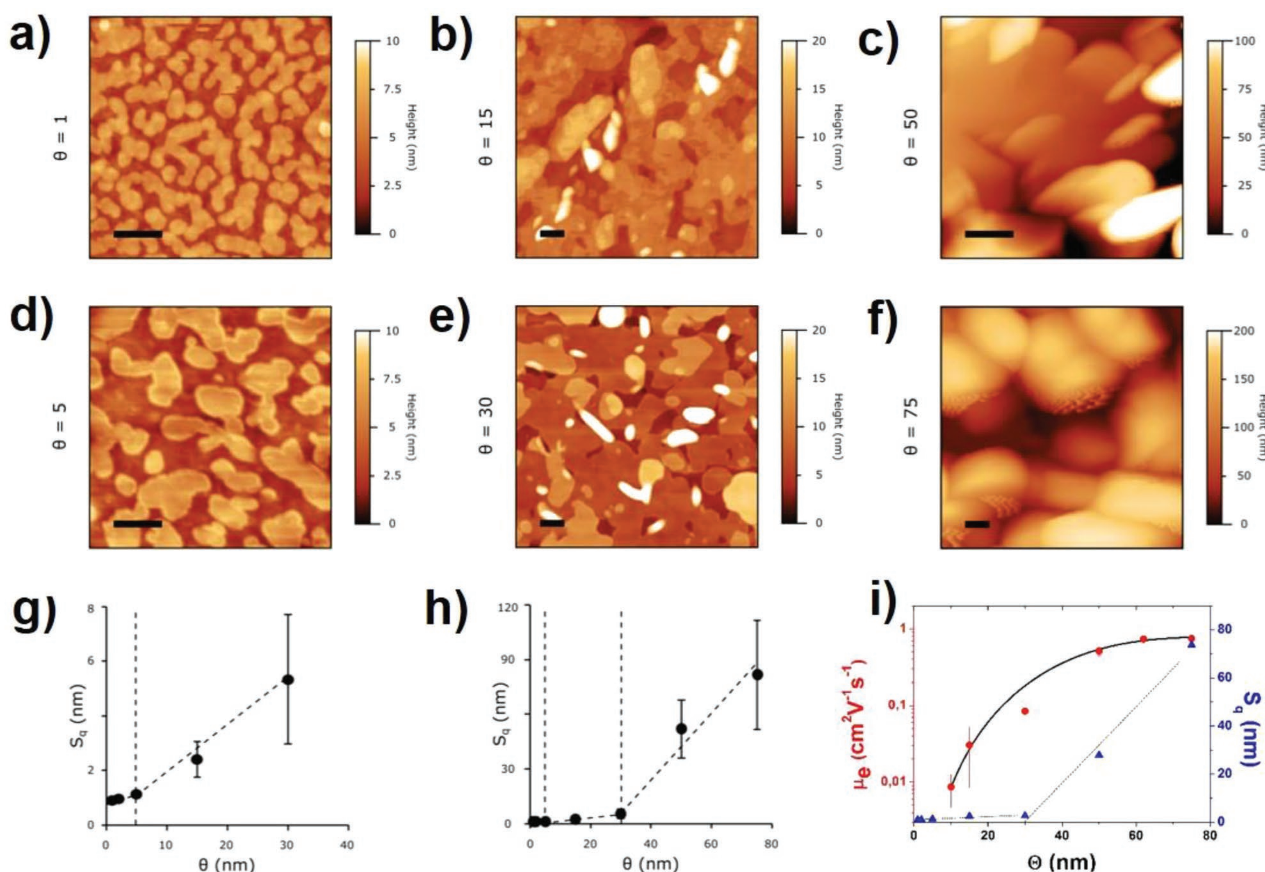

Figure 2. Morphology of NT4N thin films on PMMA at various nominal deposition thickness (Θ) values. a–f) Representative AFM images taken on samples at increasing Θ values. Scale bars are 100 nm. AFM images on (a,d) the left, (b,e) center, and (c,f) right columns correspond to 2D, mixed, and 3D growing regimes, respectively. g,h) Dependence of the root-mean-square (rms) surface roughness parameter S_q versus Θ in (g) the $1 \leq \Theta \leq 30$ nm range and (h) the $1 \leq \Theta \leq 75$ nm range. Dashed lines are linear fits with $R^2 \geq 0.97$. (h) A dramatic transition can be detected at Θ = 30 nm, while (g) a less pronounced regime change occurs at Θ = 5 nm. i) Electron mobility and S_q roughness versus film thickness: electron mobility in the saturation regime (left, red dots), and rms surface roughness (right, blue triangles) extracted from AFM imaging analysis, as a function of the thickness of the NT4N film.

semiconductor mobility. Consequently, the increase of current and charge mobility at higher NT4N thickness is not due to a more effective contact-formation between gold and NT4N, i.e., more efficient current injection and/or less contact resistance,[38] but is directly ascribable to the improvement of the transport properties in the channel region.

Since the electrode–semiconductor interface has a marginal impact on the electrical performance of the devices, we investigated the dependence of the active layer surface morphology as a function of the nominal organic film thickness (Θ) via AFM imaging and morphometry (see **Figure 2**).

For Θ values ranging from 1 to 75 nm, NT4N growth is observed to follow three distinct regimes. At very low Θ values (1–5 nm, see Figure 2 panels a and d; 2 nm, see Figure S4 in the Supporting Information), the deposition process largely follows a layer-by-layer (Frank-van der Merwe) regime with individual layers being almost fully completed prior to the formation of overlying ones. At higher Θ values (50–75 nm), NT4N is instead deposited following a 3D growth mode, which is responsible for the formation of elongated grains with heights reaching ≈300% of the nominal thickness (see Figure 2c,f). These grains cover 51% of the surface at Θ = 50 nm and have heights in the range of 30–60 nm, while at Θ = 75 nm they cover 92% of the surface and reach heights of ≈100 nm. No image of samples at Θ = 100 nm is shown in Figure 2 since the complete 3D morphology of the resulting film did not allow to perform reliable AFM analysis. A transient regime of concurrent 2D and 3D growth can be observed at intermediate Θ values (between 15 and 30 nm, see Figure 2b,e).

The root mean square surface roughness parameter S_q is a convenient morphological descriptor that is widely used for the quantitative characterization of surface growth processes.[39,40] Plotting S_q against Θ enables to quantitatively discern the three growth regimes mentioned above (see Figure 2g,h): as expected, each growth mode corresponds to a specific linear slope on this graph. The observed S_q trend can be explained by a marginally nonideal Stranski–Krastanov model (i.e., preferential 2D and 3D growth modes occurring, respectively, below and above a critical thickness Θ_C), as expected for well-known organic semiconductors (OSCs) used as active materials in FETs.[41,42] The deviation from ideality is represented by the fact that instead of a sharp transition between 2D and 3D growth modes occurring at Θ_C, we observe two transitions at $\Theta_{C1} = 5$ nm (Figure 2g) and

© 2022 The Authors. Advanced Electronic Materials published by Wiley-VCH GmbH

2199160x, 2023, 1, Downloaded from https://onlinelibrary.wiley.com/doi/10.1002/aelm.202200547 by Test, Wiley Online Library on [15/03/2023]. See the Terms and Conditions (https://onlinelibrary.wiley.com/terms-and-conditions) on Wiley Online Library for rules of use; OA articles are governed by the applicable Creative Commons License

Θ_{C2} = 30 nm (Figure 2h) covering a regime in which the two modes coexist.

The average terrace height as measured via AFM quantitative morphometry for Θ values in the range of 1–30 nm thickness was measured to be 2.2 ± 0.3 nm. This value is consistent with previous studies demonstrating that deposited NT4N molecules arrange almost perpendicular to the substrate, assuming a π-stack packing resulting in a thickness of 2.46 nm for a NT4N ML (while the molecular length is 2.8 nm).[30]

In order to correlate the NT4N growth modality displayed by the morphological features of the active layer with the electrical characteristics of the OLETs, we compared S_q values with the charge carrier mobility as the NT4N layer thickness increases (see Figure 2i). Interestingly, a drastic enhancement of the mobility occurs in the thickness range between 30 and 50 nm where the fully 3D growth mode starts.

The experimental electron mobility values reported in Table 1 were fitted by using Equation (1)[6,9,43,44]

$$\mu \approx \mu_{sat}\left[1-e^{-(\Theta/\Theta_{sat})^{\gamma}}\right] \quad (1)$$

where μ_{sat} and Θ_{sat} are the saturated charge carrier mobility and the film thickness at which the mobility saturates, respectively. The exponent γ denotes the degree of localization of the charge carriers into the electrical pathways.[43] In respect of prototypal linear conjugated compounds reported in literature,[6,44] the functional dependence of the NT4N FET mobility on the layer thickness is well described by Equation (1), but the extracted values of Θ_{sat} and γ are out of the trends. Indeed, we determine a very high value of Θ_{sat} (52 nm) combined with high mobility (μ_{sat} = 0.86 cm^2 V^{-1} s^{-1}) together with γ = 2.7 that indicates 3D percolation of charge carriers in the device.[6]

The saturation of the charge mobility is reached at very high active layer thickness (i.e., 50 nm corresponding to around 20 layer) and is also correlated with a predominant 3D growth modality. In the layer thickness range higher than 30 nm, μ_e increases with increasing S_q until it reaches a saturation value at 50 nm. This experimental finding is in contrast with the charge-carrier confinement in OSCs which is expected to be confined in the first two to three MLs close to the interface with the dielectrics in highly connected laterally extended thin films.[11,45]

Moreover, we observe that also the collected drain–source current is strictly correlated with the active-layer thickness, showing an initial linear increase with the layer thickness up to 50 nm and then saturating at higher layer-thickness values as in the case of the charge mobility (see Figure S3 in the Supporting Information). Moreover, if we consider light formation processes within the active layer, electroluminescence is nonnegligible only for semiconductor-layer thickness higher than 50 nm and the optical power linearly increases with the increasing layer thickness as in the case of source–drain current and charge mobility (see Figure S3 in the Supporting Information).

In order to shed light into the layer-dependent domain structure in OSC layer with different thickness and to collect structural information at thicknesses higher than 50 nm, at which AFM measurements become increasingly less reliable, we implemented GISAXS and GIWAXS as experimental techniques capable of detecting in-plane and out-of-plane domain size and crystallite orientation in thin films. Particularly GIWAXS is well suited to study the internal structure and degree of order in films for OFET applications.[46]

Upon deposition of the NT4N molecules, two clear diffraction spots aligned along the perpendicular direction (q_z) appear in the GISAXS patterns, with position q_z = 2.53 nm^{-1} and q_z = 5.08 nm^{-1} (see Figure S6 in the Supporting Information). The spacing for these two signals is 2.48 and 1.24 nm, which is very close to one time and half-time the NT4N long molecular axis, respectively. These two signals can be identified as the 001 and 002 reflections of the NT4N structure.[30] As expected, the sharpness and the intensity of these two signals increase with increasing the amount of deposited material (see Figure S6c in the Supporting Information). However, some interesting differences can be noticed depending on the thickness of the deposited films. The 001 and 002 reflections remain very broad until Θ ≤ 5 nm, due to the fact that the crystalline structure is not largely extended along the direction perpendicular to the substrate. For Θ ≥ 15 nm, the 001 and 002 diffraction peaks appear much sharper, and the peak intensity and sharpness increase with the film thickness. The anisotropic nature of these reflections indicates that the crystallites grow preferentially with the molecular long axis oriented almost perpendicular to the substrate (see Figure 1c).

The GISAXS signal in the direction parallel to the film surface (q_y) is correlated with the average distance between the growing NT4N islands by means of the Fourier transform.[47] In the case of low-thickness films, the inter-island distance can be estimated to be around 100 nm for Θ = 2 nm and 190 nm for Θ = 5 nm, compatible with the characteristic length scales observed above by AFM. The cross-correlation between indicators measured by topography and derived by structural analysis indicates that laterally extended islands are comprised in a single crystalline domain.[48]

The preferential orientation of growth of the crystallites and the crystalline order in the films can be studied by GIWAXS. Several diffraction spots are observed for Θ ≥ 15 nm thus indicating the NT4N crystallite growth with a high degree of internal order (see Figure S7 in the Supporting Information). Although the quality of the images is not sufficient to refine the structure with high accuracy, the comparison between experimental and simulated diffraction peak positions for the 50 and 75 nm thick films suggests that the NT4N molecules pack with a trigonal unit cell with parameters a = 0.51 nm, b = 0.55 nm, c = 2.4 nm, α = 90°, β = 93°, and γ = 89°. These values are in good agreement with the unit cell parameters reported for the NT4N single crystal in their β-phase.[32] The orientation of the diffracted spots clearly suggests that the crystallites are collectively oriented with their 00l planes parallel to the substrate. Moreover, the orientational distribution of the NT4N crystallites can be quantified by cross-correlating GISAXS and GIWAXS measurements. While for thicknesses Θ < 50 nm, the 001 reflection has the characteristic shape of a well-defined diffraction spot, for Θ ≥ 50 nm, this peak shows nonnegligible angular spreading and tends to resemble to an arc. This observation suggests qualitatively that for thicknesses Θ ≥ 50 nm the uppermost molecules do not align efficiently with respect to

© 2022 The Authors. Advanced Electronic Materials published by Wiley-VCH GmbH

2199160x, 2023, 1, Downloaded from https://onlinelibrary.wiley.com/doi/10.1002/aelm.202200547 by Test, Wiley Online Library on [15/03/2023]. See the Terms and Conditions (https://onlinelibrary.wiley.com/terms-and-conditions) on Wiley Online Library for rules of use; OA articles are governed by the applicable Creative Commons License

2199160x, 2023, 1, Downloaded from https://onlinelibrary.wiley.com/doi/10.1002/aelm.202200547 by Test, Wiley Online Library on [15/03/2023]. See the Terms and Conditions (https://onlinelibrary.wiley.com/terms-and-conditions) on Wiley Online Library for rules of use; OA articles are governed by the applicable Creative Commons License

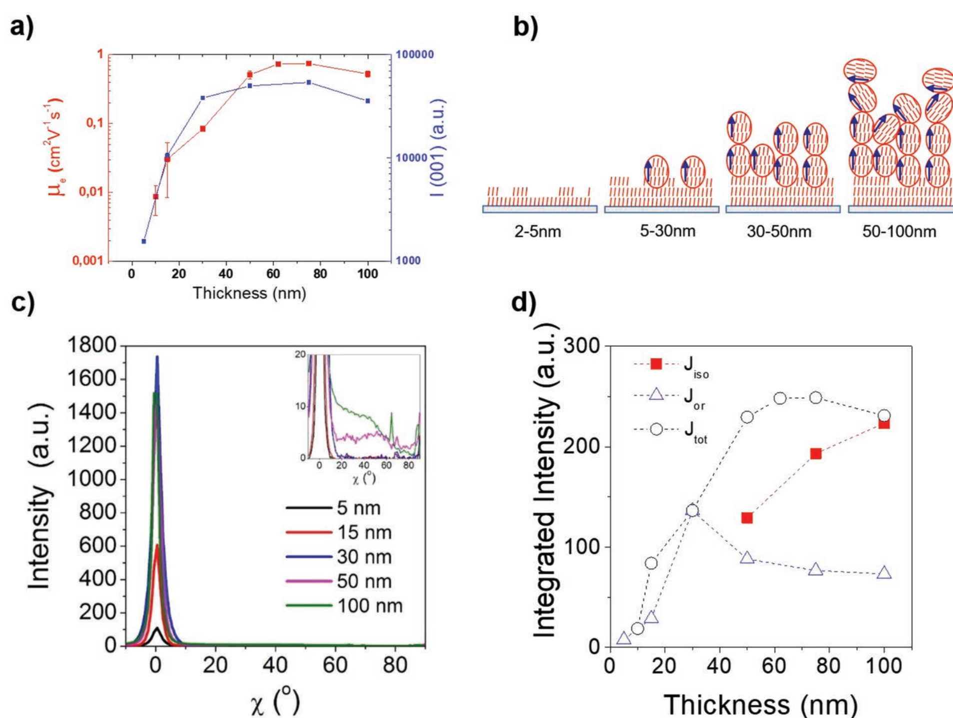

Figure 3. a) Thickness dependence of the electron mobility in saturation regime (left y-axis, red dots) and of the intensity of the 001 reflection along q_z (measured at $\alpha_i = 0.45°$, right y-axis, blue squared). Analysis of the NT4N crystals orientation. b) Schematic of the NT4N growth at different thickness as derived from the GISAXS/GIWAXS analysis. c) Pole figures extracted from the GISAXS patterns for the 001 reflection as a function of the film thickness. d) Integrated intensities for the contributions of the highly oriented structures J_{or} (open triangles) and the less aligned structures J_{iso} (squares). The total integrated intensity is also reported J_{tot}.

the substrate. The intensity of the diffraction peaks scale with the amount of deposited material and with the degree of order. Interestingly, a clear correlation can be observed between the trend of charge-carrier mobility and the variation of the intensity of the 001 peak in the GISAXS/GIWAXS measurements (see **Figure 3**a). It is worth to note that $\Theta = 50$ nm is close to the extrapolated layer thickness at which the charge mobility values saturate (Θ_{sat}).

In order to quantify the orientation of the crystalline material as a function of the active layer thickness, a more quantitative analysis was performed. GISAXS and GIWAXS data can be used to assess the fraction of the deposited material that is structurally oriented by using the so-called pole figures.[49] It was demonstrated that approximated pole figures directly extracted from a single GISAXS (or GIWAXS) pattern acquired at a fixed incident angle (α_i) can be used effectively and reliably.[50] The approximated pole figures as a function of the polar angle χ and for samples of different thickness Θ are then extracted around the 001 reflection from the GISAXS spectra (Figure 3c). The integrated area of the pole figure profiles is proportional to the fraction of the collectively oriented crystallites. Initially, increasing the film thickness from 2 to 30 nm, the approximated pole figures for the 001 peak only show a strong signal centered at around $\chi = 0°$. In addition, for thickness of 50 nm and higher (i.e., the layer thickness correlated with the prevailing 3D-growth modality), a second broader and less intense contribution to the pole figure profiles starts to appear in the range $20° < \chi < 80°$ (see the inset in Figure 3c). It can be inferred that the contribution at $\chi = 0°$ is related only to highly oriented domains (i.e., crystallites with the *c*-axis aligned almost normal to the substrate surface), while the crystalline domains with a more isotropic orientation with respect to the q_z direction contribute to the broader signal at higher polar angles. The pole figures can be further analyzed by fitting the total curve using two Lorentzian curves, whose integrals allow us to calculate the integrated intensities for the two contributions J_{or} and J_{iso}, which provide a quantitative indication of aligned and more isotropically oriented crystalline domains, respectively (see Figure 3d). Up to a thickness of 30 nm, the NT4N molecules proceeded in forming only crystallites highly aligned with the molecules in the so-called edge-on orientation and the long axis almost perpendicular to the substrate. Indeed, at this specific active-layer thickness, a more-than-one-order-of-magnitude increase in both the electron and hole mobility is observed. At higher thicknesses, crystallites with a more isotropic orientation are observed and a considerable amount of molecules with orientation different than perpendicular to the substrate is deposited. This structural information is correlated with the change in the active layer morphologies due to the transition from nonideal Stranski–Krastanov to complete 3D growth modality for thicknesses larger than 30 nm as evidenced by AFM analysis discussed above.

Thus, the X-ray scattering results here reported suggest that the saturation of the charge carrier mobility occurs when the molecular units start to arrange isotropically on top of the already deposited molecular layers instead of collectively

 © 2022 The Authors. Advanced Electronic Materials published by Wiley-VCH GmbH

maintain an edge-on molecular packing in the crystalline domains (see Figure 3a).

To further support the conclusions based on electrical and structural experimental results, we implemented a two-step multiscale simulation (details in the Experimental Section) in order to determine the expected charge mobility values in the NT4N thin-film system and second to estimate the electrical figures of merit (charge-carrier mobility, source–drain current, and threshold voltage) once the thickness-varying NT4N films are introduced in a top-contact/bottom-gate field-effect transistor platform. The approach that we implemented does not consider the thickness-varying morphology of the NT4N molecular system since we are interested to assess whether the out-of-plane orientational order in NT4N crystallites is the major driving force of the thickness-dependent saturation of charge transport.

Given that X-ray analysis demonstrates that the NT4N molecules arrange i) in an edge-on modality with respect to the substrate and ii) with a structure comparable to the β phase of the NT4N single crystals,[32] the NT4N molecular system considered for the simulation is a stack of *ab* planes along the *c* direction obtained by suitably orienting the β crystalline form with respect to the dielectric/semiconductor interface (see Figure 1c). Modeling was carried out in the framework of the nonadiabatic hopping mechanism.[51] Then, the electric field is applied along the charge-transport direction, parallel to the plane between the organic semiconductor and the dielectric.

In this configuration, the calculated charge-carrier mobility is in good accordance with the experimental values reported in Table 1: the largest mobilities predicted by Kinetic Monte Carlo simulations, for electrons and holes were 0.80 and 0.04 $cm^2 V^{-1} s^{-1}$, respectively (see Table S1 in the Supporting Information). Although the experimental mobilities are measured in field-effect configuration and not by time-of-flight experiments, the electric field used for the simulations is applied along the direction equivalent to the organic semiconductor/dielectric interface in NT4N-based FET devices, thus the comparison between the dataset is consistent.

In the case of bulk single-crystal approach that we adopt, significant electronic couplings (see Figure S9 and Table S3 in the Supporting Information) are computed only for charge pathways in the *ab* plane which is parallel to the dielectric surface, while negligible couplings are obtained in the direction perpendicular to the substrate. However, in thin-film systems the probability for charges to be transferred from one layer to a superimposed one is modulated by the transport rate across domain boundaries of the first layer and enhanced by the fact that the contact area between first and second layer is large compared to the longitudinal cross-section.[41]

To further understand the relationship between the source–drain current and the thickness of the active layer, we applied 2D device-scale drift-diffusion simulations to understand the electrical behavior of the device. For this work, we adapted the open-source model gpvdm[52,53] which solves the carrier continuity, transport, and Poisson's equations to model current flow and electrostatic effects in the device. Charge carrier trapping was accounted for using a dynamic Shockley–Read–Hall trapping/recombination model. The simulations were performed for organic semiconductor layers ranging from 30 to 100 nm thick, which represent the critical experimental thickness. This approach allowed us to decouple and understand the various physical phenomena and their contribution to the saturation transfer characteristics of the devices as a function of active layer thickness.

We found that the model was able to reproduce the relationship between experimental source–drain current curves and capture the most relevant features of the saturation transfer characteristics as a function of active layer thickness (see Figure S11 and Tables S6 and S7 in the Supporting Information). The model reproduced quantitatively the onset of currents in the 20–30 V gate bias regime, corresponding to the threshold values. The slight change in the slope of the logarithm of the current at about 50 V gate bias in $V_{GS} = V_{DS}$ curves is also correctly reproduced. In the range of thickness from 30 to 75 nm, the increase in the field-effect current by growing the thickness of the active layer can be related to the decrease in the concentration of charge carrier traps and interface dipoles (see Tables S6, S7 and Figure S13 in the Supporting Information) introduced in the simulations. The density of charge carrier trap states and interface dipoles are the phenomenological parameters associated with the intrinsic crystalline order and packing in the NT4N layer and at the interface with the dielectrics, respectively. We found that by keeping all electrical parameters constant and simply decreasing the density of trap states and the interface dipole as the active layer became thinner, the saturation transfer characteristics are reproduced as a function of thickness. This decrease may correlate with the increased size of 3D domains above the nominal thickness of 30 nm.

The simulations also show that the increase in the field-effect current with the thickness of the active layer, in the range from 30 to 75 nm, is accompanied by a slight increase of the charge density in the direction normal to the dielectric layer and thus to the in-plane charge-transport direction (see **Figure 4**). Therefore, the enhancement of molecular packing in the active layer enables the development of regions for the transport of charge carriers that extend slightly toward the bulk of the organic semiconductor, contributing to the increase of the observed current. Moreover, for a thickness of the NT4N layer ranging from 75 to 100 nm, the simulated charge density is essentially unchanged, thus further supporting the experimental findings.

We stress that the occurrence of this effect is related to the peculiar features of the NT4N layer. As a comparison, experimental characterization and simulations were also carried out for a set of devices fabricated with a prototypical n-type semiconductor (*N,N*′-dioctyl-3,4,9,10-perylenedicarboximide, PTCDI-C13) that presents similar highest occupied molecular orbital (HOMO) and lowest unoccupied molecular orbital (LUMO) levels with respect to NT4N.[38] Calculations on models of PTCDI-C13 devices performed by applying the same physical models and parameters used for the simulation of NT4N devices and keeping a constant concentration of traps and interface dipoles produced an essentially constant current irrespective of the thickness of the active layer, in excellent agreement with the experiments (see Figure S12 and Tables S8 and S9 in the Supporting Information).

 © 2022 The Authors. Advanced Electronic Materials published by Wiley-VCH GmbH

2199160x, 2023, 1, Downloaded from https://onlinelibrary.wiley.com/doi/10.1002/aelm.202200547 by Test, Wiley Online Library on [15/03/2023]. See the Terms and Conditions (https://onlinelibrary.wiley.com/terms-and-conditions) on Wiley Online Library for rules of use; OA articles are governed by the applicable Creative Commons License

2199160x, 2023, 1, Downloaded from https://onlinelibrary.wiley.com/doi/10.1002/aelm.202200547 by Test, Wiley Online Library on [15/03/2023]. See the Terms and Conditions (https://onlinelibrary.wiley.com/terms-and-conditions) on Wiley Online Library for rules of use; OA articles are governed by the applicable Creative Commons License

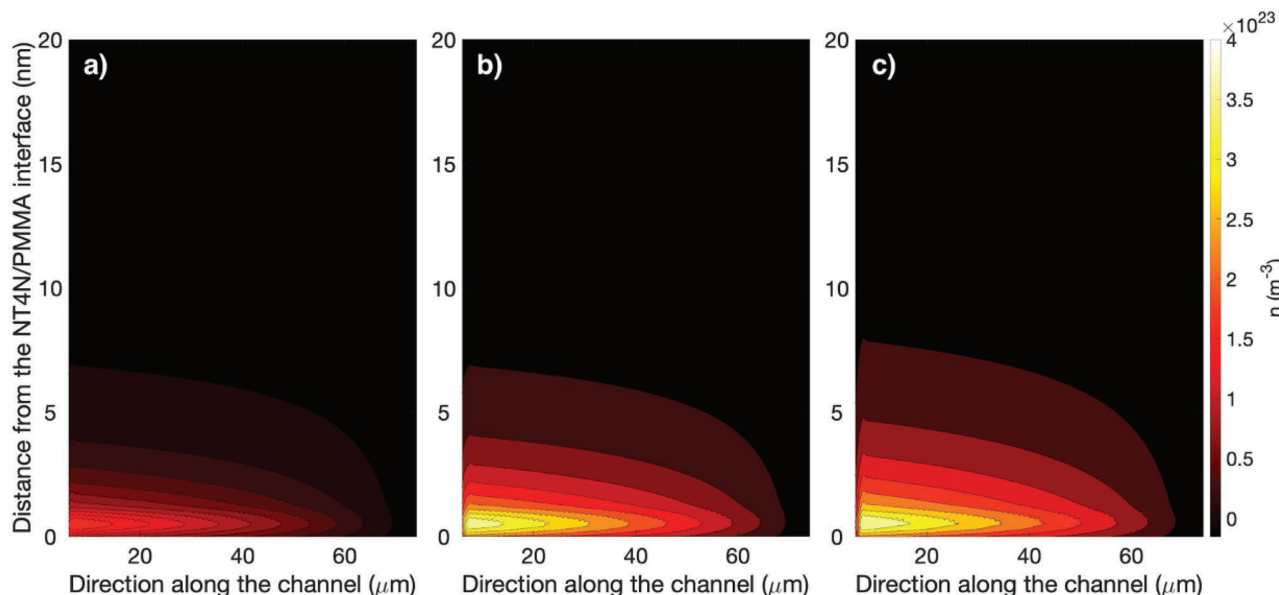

Figure 4. Charge density color map of NT4N-based OFET devices with the thickness of the active layer of a) 30 nm; b) 75 nm; c) 100 nm. Only the 20 nm region in contact with the dielectric layer is shown.

3. Conclusions

In this work, we report a comprehensive study on the interplay between charge transport, molecular packing, crystalline orientation, and growth modality in a multifunctional molecular system used as active layer in optoelectronic field-effect transistors. The functional correlation between charge mobility and a set of relevant morphological and structural indicators, such as surface roughness and crystallite orientation, is observed in the device active layer as the thickness of the thin film is increased beyond the 2D limit. We evidenced two main factors playing a crucial role in the optoelectronic performance of devices: i) the evolution of the growth modality from 2D to prevailing 3D with saturated charge mobility of about 1 $cm^2 V^{-1} s^{-1}$ at very high film thickness (≈20 ML), and ii) the high orientational order of the crystallite domains along the direction normal to the substrate even in prevailing 3D architecture.

Having discarded the contribution to charge-transport process from the injecting electrodes, we have reported clear evidence that the maximization of field-effect mobility and source–drain current in OFETs is not strictly related to preservation of multistack layer-by-layer growth. Indeed, while it is widely accepted, e.g., in the case of pentacene, that a 3D growth mode degrades charge transport,[44] here we have demonstrated for the first time that even a 3D grain-like morphology can enable high-performing field-effect devices, if the molecular orientational order in crystallites of the active layer is collectively maintained. Indeed, while pentacene shows a gradually in-plane tilt of the molecules with a thickness-driven phase transition,[54] NT4N maintains the same crystal packing (β phase) even at high thickness. The saturation of the measured field-effect charge mobility and source–drain current takes place when the molecular edge-on orientation is lost, and the crystallites tend to lay flat on the underlying film structure.

The multiscale simulation of the ambipolar charge mobility of the NT4N system modeled according to the crystalline β phase with stacks of planes normal to the *c*-axis, arranged parallel to the substrate and introduced as a thickness-varying active layer in a field-effect transistor configuration, provides a further confirmation of the proposed picture. In addition, a full-scale drift-diffusion phenomenological model has been used to gain insight into the thickness-dependent vertical charge distribution, showing an increase of the charge density toward the bulk of the film as the film thickness increases.

Overall, these results demonstrate that it is necessary to go beyond the 2D paradigm to describe the fundamental mechanisms of field-effect charge transport in OFETs and show that the out-of-plane domain size and crystallite orientation in polycrystalline films must be carefully considered to fully exploit the intrinsic properties of the semiconductors used as active layer in multifunctional OFETs.

4. Experimental Section

Device Fabrication and Characterization: NT4N powder was synthesized as described by Melucci et al.,[30] and repeated purification steps were carried out in order to guarantee a high level of purity.

Bottom gate-top contact NT4N-based OLETs were fabricated by thermal sublimation onto glass/patterned-indium tin oxide (ITO, gate contact, 150 nm)/poly(methyl methacrylate) (PMMA) (dielectric, 450 nm) substrates. Before the deposition of PMMA, the substrates were cleaned by ultrasonic bath in acetone followed by 2-propanol and dried under nitrogen flow. Finally, top Au electrodes were deposited by thermal evaporation using shadow mask.

Optoelectronic characterization was performed inside a glove box, under controlled atmosphere of nitrogen, by using a manual probe station SüssMicroTech PM5 connected to a semiconductor device parameter analyzer (Agilent B1500A) endowed with a Hamamatsu silicon photodiode (sensitivity of 0.38 AW^{-1} at 600 nm) for collecting

 © 2022 The Authors. Advanced Electronic Materials published by Wiley-VCH GmbH

photons emitted through the device glass substrate. The field-effect mobility in the saturation regime was calculated using the equation $I_{DS} = (W/2L)C_i\ \mu(V_{GS} - V_{th})^2$, where C_i is the capacitance per unit area of the insulating layer and V_{th} is the threshold voltage extracted from the square root of the drain current ($I_{DS}^{1/2}$) versus the source–gate voltage (V_{GS}) characteristics.

The contact resistance (R_C) at the Au electrodes/NT4N interface and the OLET channel resistance (R_{Ch}) were quantified at different NT4N layer thickness. R_{Ch} represents the OLETs field-effect conduction properties and, in strong accumulation condition, it could be calculated as

$$R_{Ch} = \frac{1}{\left(W/L\right)\mu C_i\left(V_{GS} - V_{th}\right)} \tag{2}$$

R_C describes the voltage drop at the injecting electrode and it was estimated using the single-transistor method proposed by Torricelli et al.[35] and further refined by least-squares regression. The values of R_C and R_{Ch} were calculated for $V_{GS} = 100$ V.

AFM Characterization: Thin film morphology was investigated by AFM imaging through a Smena NT-MDT microscope equipped with NSG10 cantilevers. Images were collected in tapping mode in air. Image processing and analysis were performed with Gwyddion v2.48.[55]

X-Ray Characterization: Film-structure evolution was investigated by performing GISAXS and GIWAXS measurements at the beamline BM26B at the European Synchrotron Radiation Facility (ESRF), Grenoble (France).[56,57]

The X-ray wavelength used for both GISAXS and GIWAXS was $\lambda = 1$ Å. GISAXS measurements were carried out using a sample-to-detector distance of 2 m. GISAXS patterns were acquired using a Pilatus1M detector with pixel size of 172 × 172 µm. Scattering from the air background was removed and the patterns were all normalized for the incoming beam intensity and for the exposure time. A double beamstop configuration was used for the samples 5–50 nm thick, while a rod-like beamstop was used for the 100 nm sample. A shorted sample-to-detector distance of 1.3 m was used for the 100 nm sample. Silver behenate was used as a standard to calibrate the GISAXS angular range. Images were acquired using two different incident angles 0.15° and 0.45°. GIWAXS measurements were carried out using a sample-to-detector distance of 125 mm. GIWAXS patterns were acquired using a Frelon2K CCD detector with pixel size of 98.3 µm. Each pattern was corrected for the dark current, detector efficiency, and beam polarization.

Here, the conventional gracing incidence notation was used where the scattering vector components were defined as

$$q_x = 2\pi/\lambda\left[\cos(2\theta_f)\cos(\alpha_f) - \cos(\alpha_i)\right] \tag{3}$$

$$q_y = 2\pi/\lambda\left[\sin(2\theta_f)\cos(\alpha_f)\right] \tag{4}$$

$$q_z = 2\pi/\lambda\left[\sin(\alpha_f) + \sin(\alpha_i)\right] \tag{5}$$

where α_i, α_f, and $2\theta_f$ are the incident, the exit angle in the vertical direction, and the exit angle in the horizontal direction, respectively. *x*, *y*, and *z* are the directions along, across horizontally, and across vertically of the X-ray beam direction, respectively. Note that for the GISAXS experiments, the q_x component along the X-ray direction could be neglected due to the small angle approximation.

The conversion from pixels to exit angles and all the intensity cuts were performed using Matlab macros.

According to the literature,[50] the integrated intensities for the oriented and the more isotropic structures were calculated as follows

$$J_{or} = \int_{\Delta\chi} I_{or}(\chi)\sin\chi d\chi \tag{6}$$

$$J_{iso} = \int_0^{90} I(\chi)\sin\chi d\chi - J_{or} \tag{7}$$

The range of integration to obtain J_{or} was $0° < \Delta\chi < 10°$.

Theoretical Calculations: Equilibrium structures of neutral and charged species were obtained from quantum chemical calculations performed at B3LYP/6-31G* level of theory. The nature of the stationary points obtained by structure optimization was assessed by vibrational frequencies calculations at the optimized structure. Vibrational frequencies were also employed to estimate the vibrational contributions to the intramolecular reorganization energy through the calculations of Huang–Rhys (HR) parameters.[58,59] All quantum-chemical calculations were performed using the Gaussian09 suite of programs.[60]

The charge transport properties were investigated within the nonadiabatic hopping mechanism.[61] The electronic couplings V_{ij} were computed at B3LYP/6-31G* level of theory, in the one-electron approximation and with the direct approach described elsewhere.[62] The energy levels and shape of frontier molecular orbitals are collected in Table S2 and Figure S8 in the Supporting Information. The gap between LUMO and LUMO+1 was ≈0.35 eV for NT4N and this pointed to a possible role of the LUMO+1 orbital beside the LUMO orbital for the n-type charge transport. For the above reason, beside the HOMO (p-type) and LUMO (n-type), the LUMO+1 orbital was also included in the calculation of electronic couplings.

The reorganization energy was composed of an intramolecular term λ_i and an "outer" contribution λ_o due to the interaction with the surrounding molecules in the crystal. λ_i was computed at B3LYP/6-31G* level of theory, either with the adiabatic potentials (AP) method (see Table S4 in the Supporting Information) or via calculations of HR parameters S_m.[2,3] In the MLJ formulation of the rate constant, λ_i collected the contribution from quantum vibrational degrees of freedom and was expressed by a single effective vibrational mode of frequency ω_{eff} and associated HR factor S_{eff}. The effective frequency ω_{eff} was determined as $\omega_{eff} = \sum_m \omega_m S_m / \sum_n S_n$. The HR factor S_{eff} was obtained from the relation $\lambda_i = \hbar\omega_{eff}S_{eff}$. Because the low-frequency vibrations could be described, to a good approximation, in classical terms, the contributions for frequencies below 150 cm^{-1} were not included in the evaluation of ω_{eff}. Their contribution was included in the λ_{class} term, summed with the outer sphere contribution λ_o assumed to be 0.01 eV according to recent studies.[63] The effective intramolecular parameters, used to evaluate rate constants, are collected in Table S5 in the Supporting Information.

Full-scale simulations of devices were performed by solving the drift-diffusion equations for majority charge carriers on a 2D discretized model of the system. All geometrical parameters were taken from the experimental configuration, apart from top electrode lengths, reduced to 5 µm (see Figure S10 in the Supporting Information). Materials parameters were determined by calibration calculations, fitting experimental saturation transfer characteristics. Currents at gate bias values below the threshold were generally ascribed to phenomena not directly related to field-effect transport (e.g., trap-assisted charge transport, leakages, etc.) and were not considered in fitting these models. All parameters used in simulations are shown in Tables S6–S9 in the Supporting Information. Calculations were performed with the gpvdm software.[52,64]

Supporting Information

Supporting Information is available from the Wiley Online Library or from the author.

Acknowledgements

This work had received funding from the European Union's Horizon 2020 research and innovation programme under grant agreement no. 780839, (MOLOKO project) grant agreement no. 101016706 (h-ALO project). The authors thank Dr. Cristiano Albonetti for fruitful scientific discussions on morphological characterization. NWO is acknowledged for providing beamtime at the ESRF.

© 2022 The Authors. Advanced Electronic Materials published by Wiley-VCH GmbH

2199160x, 2023, 1, Downloaded from https://onlinelibrary.wiley.com/doi/10.1002/aelm.202200547 by Test, Wiley Online Library on [15/03/2023]. See the Terms and Conditions (https://onlinelibrary.wiley.com/terms-and-conditions) on Wiley Online Library for rules of use; OA articles are governed by the applicable Creative Commons License

Conflict of Interest

The authors declare no conflict of interest.

Data Availability Statement

The data that support the findings of this study are available from the corresponding author upon reasonable request.

Keywords

charge transport, crystallite orientation, oligothiophenes, organic field-effect transistors, out-of-plane crystalline domains

Received: May 15, 2022
Revised: July 12, 2022
Published online: August 15, 2022

[1] S. Mao, J. Chang, H. Pu, G. Lu, Q. He, H. Zhang, J. Chen, *Chem. Soc. Rev.* **2017**, *46*, 6872.
[2] C. Vu, W. Chen, *Sensors* **2019**, *19*, 4214.
[3] M. Prosa, E. Benvenuti, D. Kallweit, P. Pellacani, M. Toerker, M. Bolognesi, L. Lopez-Sanchez, V. Ragona, F. Marabelli, S. Toffanin, *Adv. Funct. Mater.* **2021**, *31*, 2104927.
[4] S. Toffanin, V. Benfenati, A. Pistone, S. Bonetti, W. Koopman, T. Posati, A. Sagnella, M. Natali, R. Zamboni, G. Ruani, M. Muccini, *J. Mater. Chem. B* **2013**, *1*, 3850.
[5] H. Sirringhaus, *Adv. Mater.* **2014**, *26*, 1319.
[6] F. Dinelli, M. Murgia, P. Levy, M. Cavallini, F. Biscarini, D. M. De Leeuw, *Phys. Rev. Lett.* **2004**, *92*, 116802.
[7] T. Muck, V. Wagner, U. Bass, M. Leufgen, J. Geurts, L. W. Molenkamp, *Synth. Met.* **2004**, *146*, 317.
[8] W. A. Koopman, S. Toffanin, M. Natali, S. Troisi, R. Capelli, V. Biondo, A. Stefani, M. Muccini, *Nano Lett.* **2014**, *14*, 1695.
[9] B. R. Ruiz, A. Papadimitratos, A. C. Mayer, G. G. Malliaras, *Adv. Mater.* **2005**, *17*, 1795.
[10] M. Kiguchi, M. Nakayama, K. Fujiwara, K. Ueno, T. Shimada, K. Saiki, *Jpn. J. Appl. Phys., Part 2* **2003**, *42*, L1408.
[11] A. Shehu, S. D. Quiroga, P. D'Angelo, C. Albonetti, F. Borgatti, M. Murgia, A. Scorzoni, P. Stoliar, F. Biscarini, *Phys. Rev. Lett.* **2010**, *104*, 246602.
[12] J. Gao, J. B. Xu, M. Zhu, N. Ke, D. Ma, *J. Phys. D: Appl. Phys.* **2007**, *40*, 5666.
[13] E. A. You, Y. G. Ha, Y. S. Choi, J. H. Choi, *Synth. Met.* **2005**, *153*, 209.
[14] G. Generali, F. Dinelli, R. Capelli, S. Toffanin, F. Di Maria, M. Gazzano, G. Barbarella, M. Muccini, *J. Phys. Chem. C* **2011**, *115*, 23164.
[15] Y. Fan, J. Liu, W. Hu, Y. Liu, L. Jiang, *J. Mater. Chem. C* **2020**, *8*, 13154.
[16] J. Liu, Y. Yu, J. Liu, T. Li, C. Li, J. Zhang, W. Hu, Y. Liu, L. Jiang, *Adv. Mater.* **2022**, *34*, 2107574.
[17] J. Liu, L. Jiang, W. Hu, Y. Liu, D. Zhu, *Sci. China Chem.* **2019**, *62*, 313.
[18] Y. Shi, L. Jiang, J. Liu, Z. Tu, Y. Hu, Q. Wu, Y. Yi, E. Gann, C. R. McNeill, H. Li, W. Hu, D. Zhu, H. Sirringhaus, *Nat. Commun.* **2018**, *9*, 2933.
[19] F. Cicoira, C. Santato, F. Dinelli, M. Murgia, M. A. Loi, F. Biscarini, R. Zamboni, P. Heremans, M. Muccini, *Adv. Funct. Mater.* **2005**, *15*, 375.
[20] C. Wang, H. Dong, L. Jiang, W. Hu, *Chem. Soc. Rev.* **2018**, *47*, 422.
[21] L. Chua, J. Zaumseil, J. Chang, E. Ou, P. Ho, H. Sirringhaus, R. H. Friend, *Nature* **2005**, *434*, 194.
[22] A. Yamamura, S. Watanabe, M. Uno, M. Mitani, C. Mitsui, J. Tsurumi, N. Isahaya, Y. Kanaoka, T. Okamoto, J. Takeya, *Sci. Adv.* **2018**, *4*, eaao5758.
[23] J. Huang, J. Sun, H. E. Katz, *Adv. Mater.* **2008**, *20*, 2567.
[24] O. D. Jurchescu, J. Baas, T. T. M. Palstra, *Appl. Phys. Lett.* **2004**, *84*, 3061.
[25] M. Muccini, *Nat. Mater.* **2006**, *5*, 605.
[26] S. Toffanin, R. Capelli, W. Koopman, G. Generali, S. Cavallini, A. Stefani, D. Saguatti, G. Ruani, M. Muccini, *Laser Photonics Rev.* **2013**, *7*, 1011.
[27] M. Muccini, S. Toffanin, *Organic Light-Emitting Transistors: Towards the Next Generation Display Technology*, Wiley-Science, Wise Co-Publication, New York **2016**.
[28] M. Zambianchi, E. Benvenuti, C. Bettini, C. Zanardi, R. Seeber, D. Gentili, M. Cavallini, M. Muccini, V. Biondo, C. Soldano, G. Generali, S. Toffanin, M. Melucci, *J. Mater. Chem. C* **2016**, *4*, 9411.
[29] A. K. Bansal, M. T. Sajjad, F. Antolini, L. Stroea, P. Gečys, G. Raciukaitis, P. André, A. Hirzer, V. Schmidt, L. Ortolani, S. Toffanin, S. Allard, U. Scherf, I. D. W. Samuel, *Nanoscale* **2015**, *7*, 11163.
[30] M. Melucci, M. Zambianchi, L. Favaretto, M. Gazzano, A. Zanelli, M. Monari, R. Capelli, S. Troisi, S. Toffanin, M. Muccini, *Chem. Commun.* **2011**, *47*, 11840.
[31] M. Melucci, L. Favaretto, M. Zambianchi, M. Durso, M. Gazzano, A. Zanelli, M. Monari, M. G. Lobello, F. De Angelis, V. Biondo, G. Generali, S. Troisi, W. Koopman, S. Toffanin, R. Capelli, M. Muccini, *Chem. Mater.* **2013**, *25*, 668.
[32] L. Maini, F. Gallino, M. Zambianchi, M. Durso, M. Gazzano, K. Rubini, D. Gentili, I. Manet, M. Muccini, S. Toffanin, M. Cavallini, M. Melucci, *Chem. Commun.* **2015**, *51*, 2033.
[33] M. Durso, C. Bettini, A. Zanelli, M. Gazzano, M. G. Lobello, F. De Angelis, V. Biondo, D. Gentili, R. Capelli, M. Cavallini, S. Toffanin, M. Muccini, M. Melucci, *Org. Electron.* **2013**, *14*, 3089.
[34] M. Prosa, S. Moschetto, E. Benvenuti, M. Zambianchi, M. Muccini, M. Melucci, S. Toffanin, *J. Mater. Chem. C* **2020**, *8*, 15048.
[35] F. Torricelli, M. Ghittorelli, L. Colalongo, Z. M. Kovacs-Vajna, *Appl. Phys. Lett.* **2014**, *104*, 093303.
[36] E. J. Meijer, G. H. Gelinck, E. Van Veenendaal, B. H. Huisman, D. M. De Leeuw, T. M. Klapwijk, *Appl. Phys. Lett.* **2003**, *82*, 4576.
[37] D. Boudinet, M. Benwadih, S. Altazin, R. Gwoziecki, J. M. Verilhac, R. Coppard, G. L. Blevennec, I. Chartier, G. Horowitz, *Org. Electron.* **2010**, *11*, 291.
[38] M. Natali, M. Prosa, A. Longo, M. Brucale, F. Mercuri, M. Buonomo, N. Lago, E. Benvenuti, F. Prescimone, C. Bettini, A. Cester, M. Melucci, M. Muccini, S. Toffanin, *ACS Appl. Mater. Interfaces* **2020**, *12*, 30616.
[39] F. Schreiber, *Phys. Status Solidi A* **2004**, *201*, 1037.
[40] A. Brillante, I. Bilotti, R. G. Della Valle, E. Venuti, A. Girlando, M. Masino, F. Liscio, S. Milita, C. Albonetti, P. D'Angelo, A. Shehu, F. Biscarini, *Phys. Rev. B* **2012**, *85*, 195308.
[41] J. A. Venables, G. D. T. Spiller, M. Hanbucken, *Rep. Prog. Phys.* **1984**, *47*, 399.
[42] S. Kowarik, A. Gerlach, F. Schreiber, *J. Phys.: Condens. Matter* **2008**, *20*, 184005.
[43] S. W. Liu, C. C. Lee, H. L. Tai, J. M. Wen, J. H. Lee, C. T. Chen, *ACS Appl. Mater. Interfaces* **2010**, *2*, 2282.
[44] J. Shi, D.-T. Jiang, J. R. Dutcher, X.-R. Qin, *J. Vac. Sci. Technol., B* **2015**, *33*, 050604.
[45] R. Lassnig, B. Striedinger, M. Hollerer, A. Fian, B. Stadlober, A. Winkler, *J. Appl. Phys.* **2014**, *116*, 114508.
[46] J. Dong, S. Sami, D. M. Balazs, R. Alessandri, F. Jahani, L. Qiu, S. J. Marrink, R. W. A. Havenith, J. C. Hummelen, M. A. Loi, G. Portale, *J. Mater. Chem. C* **2021**, *9*, 16217.
[47] T. Salditt, T. H. Metzger, J. Peisl, B. Reinker, M. Moske, K. Samwer, *Europhys. Lett.* **1995**, *32*, 331.

© 2022 The Authors. Advanced Electronic Materials published by Wiley-VCH GmbH

2199160x, 2023, 1, Downloaded from https://onlinelibrary.wiley.com/doi/10.1002/aelm.202200547 by Test, Wiley Online Library on [15/03/2023]. See the Terms and Conditions (https://onlinelibrary.wiley.com/terms-and-conditions) on Wiley Online Library for rules of use; OA articles are governed by the applicable Creative Commons License

[48] A. Tersigni, X. R. Qin, C. Kim, R. A. Gordon, D. T. Jiang, *Phys. Rev. B* **2011**, *84*, 035303.
[49] J. L. Baker, L. H. Jimison, S. Mannsfeld, S. Volkman, S. Yin, V. Subramanian, A. Salleo, A. P. Alivisatos, M. F. Toney, *Langmuir* **2010**, *26*, 9146.
[50] J. Balko, G. Portale, R. H. Lohwasser, M. Thelakkat, T. Thurn-Albrecht, *J. Mater. Res.* **2017**, *32*, 1957.
[51] T. Vehoff, A. Troisi, D. Andrienko, *J. Am. Chem. Soc.* **2010**, *132*, 11702.
[52] N. Majeed, M. Saladina, M. Krompiec, S. Greedy, C. Deibel, R. C. I. MacKenzie, *Adv. Funct. Mater.* **2020**, *30*, 1907259.
[53] S. Solak, S. Shishegaran, A. C. Hübler, R. C. I. MacKenzie, *Sol. RRL* **2021**, *5*, 2100787.
[54] H. L. Cheng, Y. S. Mai, W. Y. Chou, L. R. Chang, X. W. Liang, *Adv. Funct. Mater.* **2007**, *17*, 3639.
[55] D. Nečas, P. Klapetek, *Cent. Eur. J. Phys.* **2012**, *10*, 181.
[56] A. J. R. Bras, E. H. W. Bras, I. P. Dolbnya, D. Detollenaere, R. van Tol, M. Malfois, G. N. Greaves, *J. Appl. Crystallogr.* **2003**, *36*, 791.
[57] G. Portale, D. Cavallo, G. C. Alfonso, D. Hermida-Merino, M. Van Drongelen, L. Balzano, G. W. M. Peters, J. G. P. Goossens, W. Bras, *J. Appl. Crystallogr.* **2013**, *46*, 1681.
[58] J. L. Brédas, D. Beljonne, V. Coropceanu, J. Cornil, *Chem. Rev.* **2004**, *104*, 4971.
[59] V. Coropceanu, J. Cornil, D. A. da Silva Filho, Y. Olivier, R. Silbey, J. L. Brédas, *Chem. Rev.* **2007**, *107*, 926.
[60] M. J. Frisch, G. W. Trucks, H. B. Schlegel, G. E. Scuseria, M. A. Robb, J. R. Cheeseman, G. Scalmani, V. Barone, B. Mennucci, G. A. Petersson, H. Nakatsuji, M. Caricato, X. Li, H. P. Hratchian, A. F. Izmaylov, J. Bloino, G. Zheng, J. L. Sonnenberg, M. Hada, M. Ehara, K. Toyota, R. Fukuda, J. Hasegawa, M. Ishida, T. Nakajima, Y. Honda, O. Kitao, H. Nakai, T. Vreven, J. A. Montgomery Jr., et al., *Gaussian 09, Revision A*, Gaussian, Inc., Wallingford, CT **2009**.
[61] A. Troisi, *Chem. Soc. Rev.* **2011**, *40*, 2347.
[62] A. Troisi, G. Orlandi, *Chem. Phys. Lett.* **2001**, *344*, 509.
[63] D. P. McMahon, A. Troisi, *J. Phys. Chem. Lett.* **2010**, *1*, 941.
[64] R. C. I. MacKenzie, T. Kirchartz, G. F. A. Dibb, J. Nelson, *J. Phys. Chem. C* **2011**, *115*, 9806.

© 2022 The Authors. Advanced Electronic Materials published by Wiley-VCH GmbH

2199160x, 2023, 1, Downloaded from https://onlinelibrary.wiley.com/doi/10.1002/aelm.202200547 by Test, Wiley Online Library on [15/03/2023]. See the Terms and Conditions (https://onlinelibrary.wiley.com/terms-and-conditions) on Wiley Online Library for rules of use; OA articles are governed by the applicable Creative Commons License